Mechanistic Insights into the Origin of Substituent-Directed Product *Z* −*E* Selectivity for Gold-Catalyzed [4+1]-Annulations of 1,4-Diyn-3-Ols with Isoxazoles: A DFT Study

Kaifeng Wang[1], Yuxia Liu[1,4*], Qiao Wu[1], Lingjun Liu[1], Yulin Li[2], Tony D. James[3], Guang Chen[1], Siwei Bi[1,*]

1 School of Chemistry and Chemical Engineering, Qufu Normal University, Qufu, 273165, P. R. China. E-mail: liuyuxia2008@163.com, siweibi@126.com, Fax: +86-537-4456305 ; Tel: +86-537-4458308

2 Key Laboratory of Tibetan Medicine Research & Qinghai Key Laboratory of Qinghai-Tibet Plateau Biological Resuorces, Northwest Institute of Plateau Biology, Chinese Academy of Science, Xining 810001, Qinghai P. R. China

3 Department of Chemistry, University of Bath, Bath, UK BA2 7AY

4 Department of Chemical Engineering and §Waterloo Institute for Nanotechnology, University of Waterloo, 200 University AvenueWest, Waterloo, Ontario, Canada, N2L 3G1

Abstract

Density functional theory (DFT) calculations were used to explore the Au(I)-catalyzed selective [4+1] annulations of cyclopropyl- and H-substituted 1,4-diyn-3-ols with isoxazole. The results indicated that the N-nucleophilic attack of isoxazole favors the π-non-phenylalkyne position of 1,4-diyn-3-ols, which can be attributed to a smaller steric hindrance involved as compared to the attack at the phenylalkyne position. After the nucleophilic attack, instead of obtaining the α–hydroxy gold carbene intermediate proposed experimentally, a concerted three-step forward product by isoxazole O-N cleavage, 1,2-phenylalkyne shift and the hydroxyl H shift was identified as the key intermediate, for the reaction proceeding either via an Au-assisted C=C double-bond rotation to produce the *Z*-isomeric enone or via two different Au-assisted C=C rotations to furnish the *E*-configured enone depending on the substituents used. Further theoretical investigations indicated that the chemoselective step is the nucleophilic cyclization but not the C=C double-bond rotation. The chemoselective preference for the *Z*-configured product using the cyclopropyl substituent was attributed to two factors: i) the additional O⋯H—N hydrogen bonding interaction stabilizes the rate-determining cyclization TS leading to the *Z*-product, and ii) further *Z*-*E* product-isomerization is blocked due to significant structural deformation being involved. In contrast, using the H substituent results in a reversed chemoselectivity with exclusive formation of the *E*-configured enones, which is closely related to the smaller entropy effects involved.

Keywords: Au(I)-catalysis, [4+1] annulation, 1,4-diyn-3-ols, selectivity, DFT

1. Introduction

Pyrrole frameworks are significant core structures for numerous bioactive and natural products [1-4], which has stimulated the development of new synthetic strategies for their formation. Gold-catalyzed annulations of unsaturated hydrocarbons with N, O-containing nucleophiles have emerged as powerful tools to access highly functionalized pyrrole heterocycles [5-11]. As a result, these reactions have attracted significant attention and have been extensively investigated. A series of gold-catalyzed [3+2]-annulations of isoxazoles or benzisoxazoles with ynamides have been evaluated by several research groups, including Ye [12-14] and Hashmi [15-16], etc. In addition, other N,O heterocyclic nucleophilies, such as 1,4,2-dioxazoles [17], 1,2,4-oxadiazoles [18] and 4,5-dihydro-1,2,4-oxadiazoles [19], have been shown to participate in these catalytic annulations with ynamides. Apart from electron-rich ynamides, the electron-deficient propiolates have been developed for the gold-catalyzed [4+1]-annulations of isoxazoles [20, 21]. However, in contrast to the annulations with reactive ynamides and propiolates, the corresponding reactions with unactivated alkynes are rarely investigated.

Recently, Liu and co-workers successfully described the gold-catalyzed [4+1]-annulation of isoxazoles or benzisoxazoles [22], in which inactive 1,4-diyn-3-ols are employed as the electrophilic reactants. These operationally simple reactions feature broad substrate scope and exhibit extraordinary chemoselectivity and regioselectivity. Scheme 1 displays the representative gold (I)-catalyzed annulations developed by Liu's group [22]. With LAuCl/AgOTf (10 mol %) (L= IPr) in hot dichloroethane (DCE) at 80˚C, the cyclopropyl-substituted 1,4-diyn-3-ol (R = cyclopropyl), **1A**, produces the *Z*-configured pyrrolyl N-enone $^{\mathbf{Z}}\mathbf{P_a}$ in a high yield. However, under the identical catalytic conditions, replacing the cyclopropyl group in **1A** by a hydrogen atom (the

substrate is denoted as **2A**) results in a different chemoselectivity: the final product being the *E*-configured enone $^{E}\mathbf{P_b}$ with an isolated yield of 64%.

Scheme 1. Au(I)-catalyzed chemoselective [4+1] annulations of representative nonsymmetric 1,4-diyn-3-ols (**A**) with,isoxazole (**B**) reported by Liu and co-workers [22].

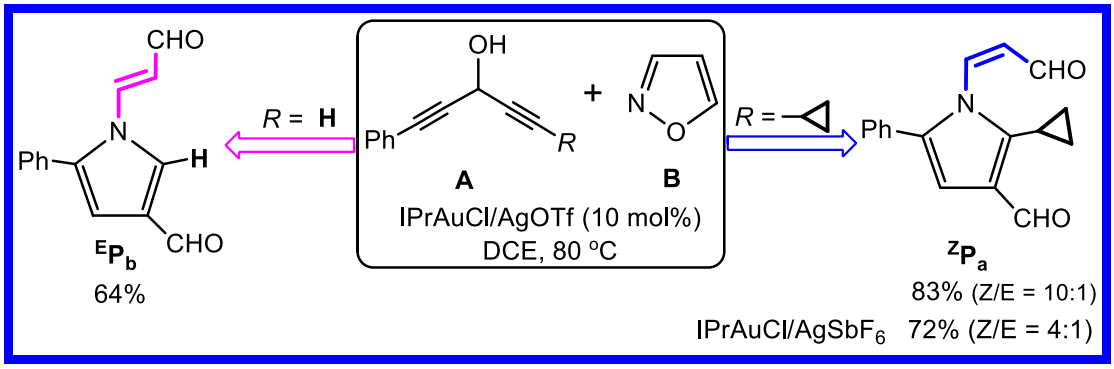

To account for these annulation reactions, plausible mechanistic pathways are proposed by Liu et al. [22] and shown in Scheme 2 with the representative substrates **1A** and **2A**, respectively. For the reaction of **1A**, the LAu^{+} π-coordinates regioselectivity with the phenylalkyne over the cyclopropylalkyne of **1A**, followed by N-nucleophilic attack of the isoxazole **B** at C^{1}, producing species **2**. The isoxazole N-O cleavage of **2** then occurs to afford α–hydroxy iminogold carbene intermediate **3**. Subsequently, 1,2-alkyne migration and protodeauration furnishes the Au-π-3-yn-1-imine adduct **5**, from which $^{Z}\mathbf{P_a}$ is ultimately produced with the dissociation of the active LAu^{+} catalyst. With the system starting with **2A**, Liu and co-workers postulated that the reaction proceeds via a similar pathway, i.e., LAu^{+} π-coordination with the terminal alkyne, nucleophilic attack of **B**, isozaxole N-O cleavage, the 1,2-alkyne migration and protodeauration, resulting in the *Z*-configured enone **8**. Liu postulates that the *E*-configured isomer $^{E}\mathbf{P_b}$ is then formed through a facile C=C double bond rotation.

Scheme 2. Postulated pathways proposed by Liu's group [22] for the Au(I)-catalyzed

[4+1] annulations of cyclopropyl- and H-substituted 1,4-diyn-3-ols with,isoxazole **B**, respectively.

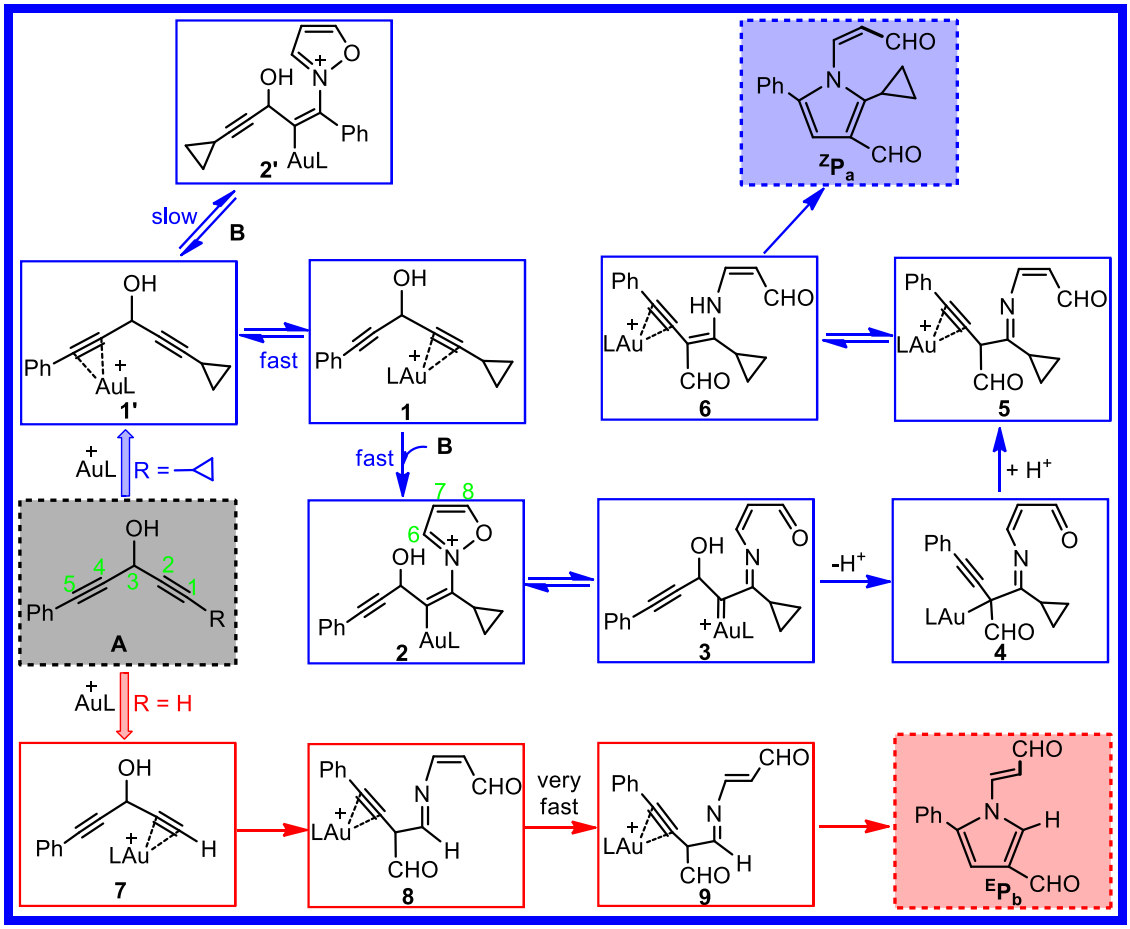

In this work, with the aid of density functional theory (DFT) calculations, we investigated these reactions in detail. For both reactions involving **1A** or **2A**, the experimentally proposed α-hydroxy iminogold carbenoid intermediate was not a local minimum. Instead, a concerted three-step forward product obtained by isoxazole O-N cleavage, 1,2-phenylalkyne shift and the hydroxyl H shift is identified as the key intermediate, from which either Au-assisted C^1=C^2 rotation provides $^{z}\mathbf{P_a}$ or Au-assisted double C=C double-bond rotation (C^6=C^7 and C^1=C^2 in order) furnishes $^{E}\mathbf{P_b}$. Based on the mechanistic details, the inherent regioselectivity and chemoselectivity have been disentangled. We believed that these in-depth analyses will inspire the development of new gold-catalyzed annulation reaction protocols.

2. Computational Details

All DFT calculations were carried out with the Gaussian 09 version [23]. The geometries of all stationary points were fully optimized in the framework of density functional theory (DFT) at the B3LYP level [24-27], which has been shown to describe Au-catalyzed and other transition-metal-catalyzed organometallic systems reasonably well [28-33]. The SDD [34, 35] basis set was chosen for Au atom whereas the 6-31g (d) basis set was used for all other atoms, including C, H, O and N atoms. All optimized stationary points were confirmed as local minima (zero imaginary frequencies) or first-order saddle points (one imaginary frequency) by performing vibrational frequencies at the same level of theory and the free energies were provided at 298.15 K. IRC [36, 37] calculations from transition states were also conducted to ensure that such structures indeed connected two relevant minima. The energies in the DCE solvent were evaluated at the M06 [38, 39] level employing a larger basis set (6-311+g(d,p)) for the non-metallic atoms and SDD basis set for Au by single-point calculations using a self-consistent reaction field (SCRF) method [40] with the PCM model [41, 42]. In addition, no entropy correction [43] is added in this paper.

3. Results and Discussion

3.1 Reactions on Cyclopropyl-Substituted Substrate 1A

3.1.1 Formation Mechanism of the N-O Cleavage Intermediate

The calculated results are given in Fig. 1. Initial LAu^+ coordination with **1A** gives the π-cyclopropylalkyne coordinated adduct **IM1**, which is exergonic by 23.0 kcal/mol. From **IM1**, through **TS1-2**, the N nucleophilic attack of **B** surmounts an energy requirement of 21.2 kcal/mol to afford **IM2**. According to the proposal in Scheme 2, after the N-nucleophilic attack, the isoxazole ring-opening by N-O cleavage takes place to deliver the α-hydroxy iminogold carbenoid **3**, which evolves into the final product

$^{Z}\mathbf{P}_{\mathbf{a}}$. However, our calculated results indicate that the proposed species **3** is not a true local minimum on the potential energy profile, which is supported by the recent work of Ariafard and co-workers [44]. Upon optimization, it always collapses into **IM3**, the forward product of a concerted three-step process, involving isoxazole O-N cleavage, 1,2-phenylalkyne shift and the hydroxyl H migration . The concerted step via **TS2-3** has a barrier of 11.3 kcal/mol and is exergonic by 45.5 kcal/mol relative to **IM2**. Therefore, in the following transformation, **IM3** was identified as the key intermediate to access $^{Z}\mathbf{P}_{\mathbf{a}}$. Note that, from **IM2** to **TS2-3**, the N⋯O distance is elongated by 0.432 Å from 1.396 Å to 1.828 Å, while both the (hydroxyl) O⋯H (from 0.973 Å to 0.971 Å) and C3⋯C4 distance (1.543 Å to 1.471 Å) vary insignificantly. These results imply that the N-O rupture might be the main driving force for the concerted three-step process.

As indicated in Fig. 1, except for π-coordinating with the cyclopropylalkyne of **1A**, LAu^{+} can π-interact with the phenylalkyne of **1A**, leading to **IM1'**, which, through **TS1-2'**, can be easily transformed into **IM1**. Unfortunately, the transition structure for the subsequent N-nucleophilic attack from **IM1'**, **TS1-2'**, is found to be 3.0 kcal/mol higher than **TS1-2** in free energy. The main reason lies in the steric repulsion between the cyclopropylalkyne moiety and the isoxazole ring in **TS1-2'**. The detailed discussions for the regioselectivity are collected into Supporting Information (Fig. S1).

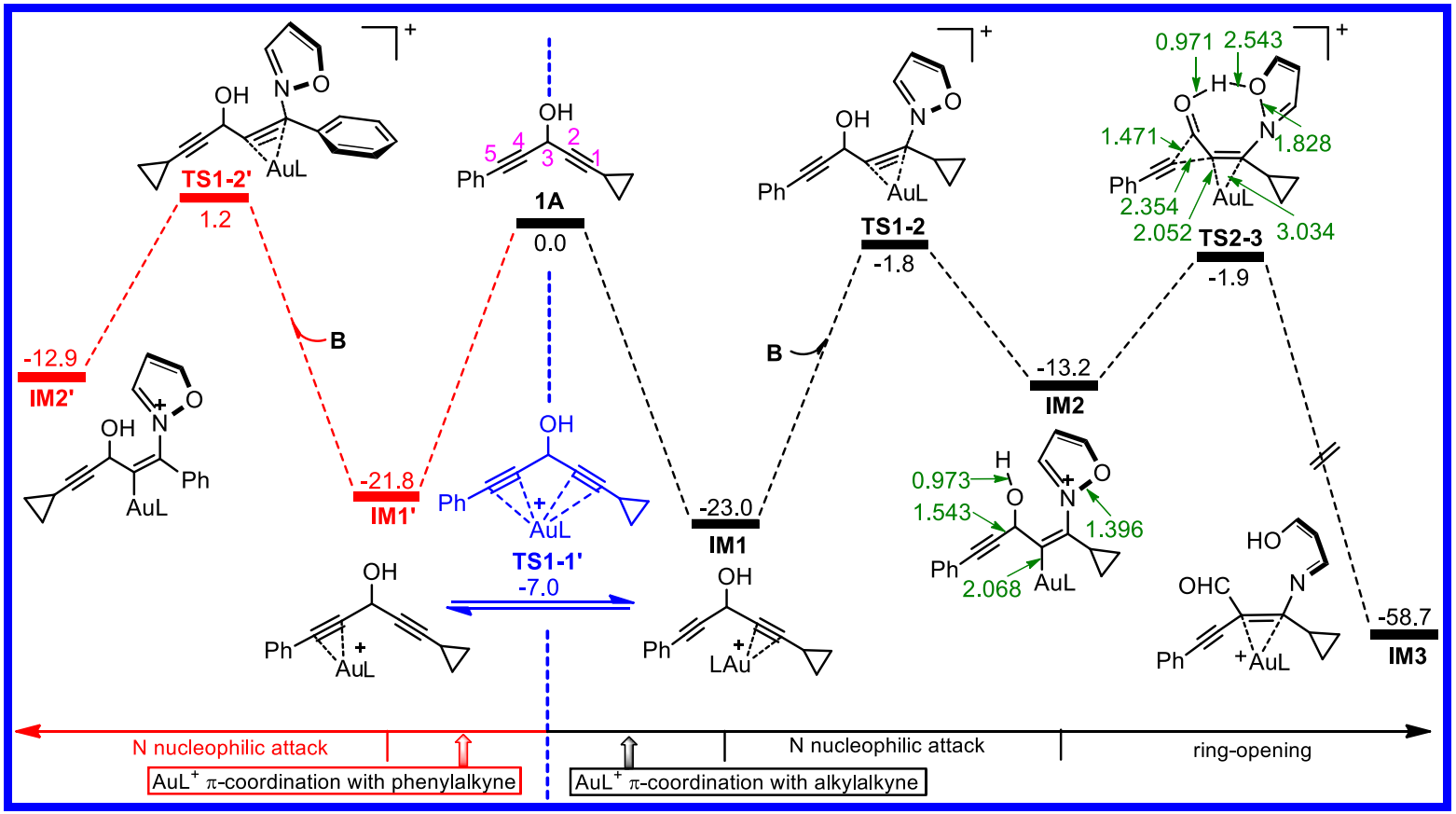

Fig. 1. Calculated free energy profiles in DCE solvent for forming the N-O cleavage intermediate **IM3** from the cyclopropyl-substituted 1,4-diyn-3-ol **1A**. The relative free energies and bond distances are given in kcal/mol and Å, respectively. L = IPr

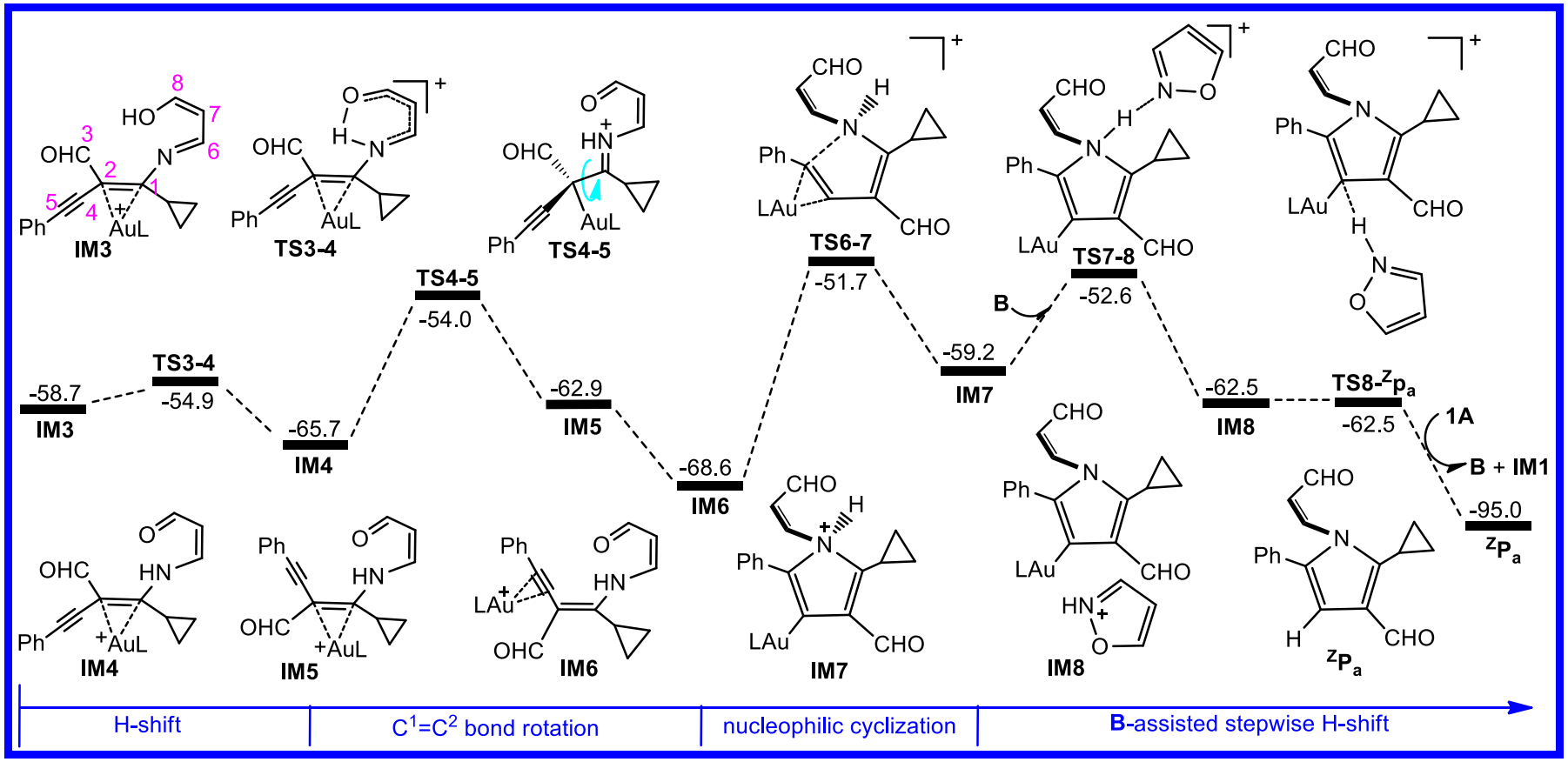

Fig. 2. Calculated free energy profile in DCE solvent for forming $^{Z}\mathbf{P_a}$ from the N-O cleavage intermediate **IM3** established in the present work. The relative free energies and bond distances are given in kcal/mol and Å, respectively. L = IPr

*3.1.2 $^{Z}P_a$ Formation Mechanism Starting from **IM3***

Fig. 2 illustrates the calculated potential energy profile for $^{Z}\mathbf{P_a}$ formation from **IM3**. The hydroxyl H atom in **IM3** performs a migration to the N atom, affording more stable intermediate **IM4**. The process via **TS3-4** is very facile with a barrier of 3.8 kcal/mol, which might be attributed to the O···H···N interaction in the transition state. In order to facilitate intramolecular N-nucleophilic attack to the C^5 atom, the C^1=C^2 double-bond in **IM4**, with the assistance of LAu^+, experiences a rotation to give the isomer **IM5**. The double-bond rotation is computed to have an unexpectedly low barrier of 11.7 kcal/mol, much lower than normal C=C rotation. It is seen in Fig. 2, that the C^1=C^2 double bond in **IM4** has been switched to an approximately C^1—C^2 single bond in **TS4-5** with a distance of 1.523 Å. Such an unexpected C=C double-bond rotation can be attributed to the presence of the LAu^+ catalyst and sp^2-N atom. For the process from **IM4** to **TS4-5**, with the C^1=C^2 bond being switched to a single bond, the C^1-N single bond is being switched to a double bond. Consequently, the N atom is positively charged and C^2 negatively charged in **TS4-5**. The positive charge on the N atom can be effectively delocalized by the adjacent sp^2-C^1 atom and vinyl aldehyde group, and simultaneously, the negative charge on C^2 can be stabilized by the LAu^+ catalyst. As a result, **TS4-5** is low in energy and enables the C^1=C^2 rotation to be readily accessible. A similar example of C=C double-bond rotation is also found in the following figures (**IM14** → **TS14-15** in Fig. 4, **IM19** → **TS19-20** in Fig. 5, **IM21** → **TS21-22** and **IM23** → **TS23-24** in Fig. 6), and other transition-metal catalyzed systems documented by several research groups [45-48] and our group [49]. From **IM5**, with LAu^+ turning to π-coordinate towards the phenylalkyne moiety, the ring-closure process by the N-nucleophilic attack to the C^5 atom occurs and provides the pyrrole cycle intermediate **IM7**. For the subsequent protodeauration, in light of the Lewis basicity of the isoxazole (**B**) N atom, we designed a stepwise isoxazole N-assisted

protodeauration to give $^{Z}\mathbf{P_a}$, which is shown in Fig. 2. The (N)H atom in **IM7** is firstly trapped by the isoxazole N atom to give **IM8**. Then, the trapped H atom transfers to the C(AuL) atom via **TS8-**$^{Z}\mathbf{Pa}$, affording the final product $^{Z}\mathbf{P_a}$ with the release of LAu^{+} and isoxazole **B**.

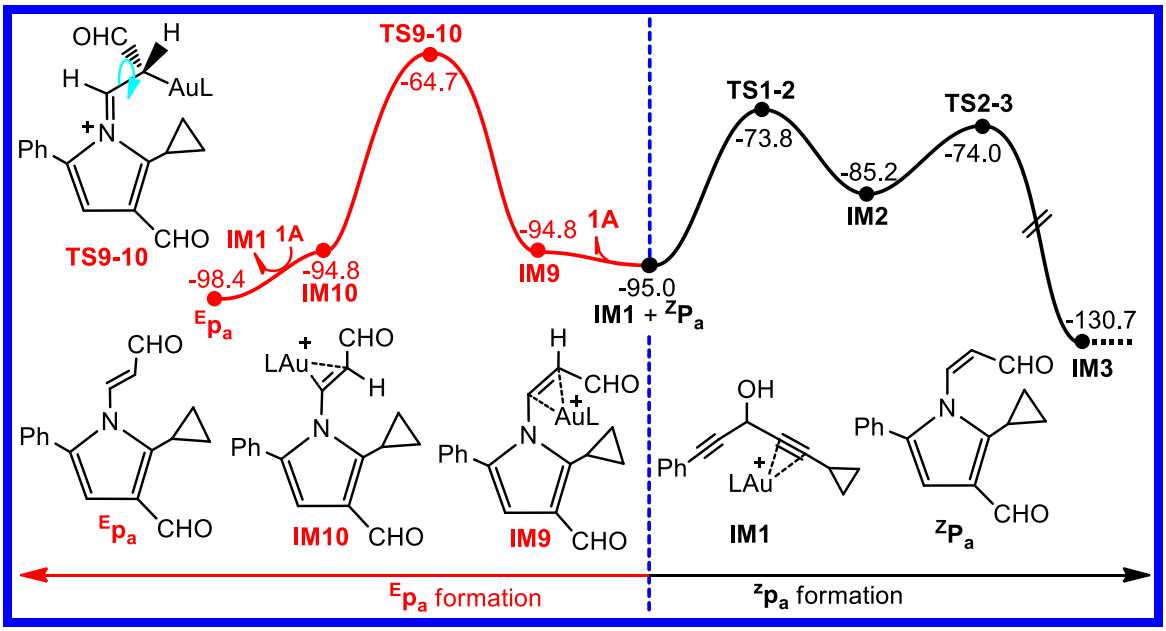

Fig. 3. Calculated free energy profiles in DCE solvent for forming $^{Z}\mathbf{P_a}$ (black line) and $^{E}\mathbf{P_a}$ via $^{Z}\mathbf{P_a}$ (red line), respectively. The relative free energies are given in kcal/mol. L = IPr

Once formed, $^{Z}\mathbf{P_a}$, through a formal C^6=C^7 double bond rotation, possibly isomerizes into the *E*-configured enone $^{E}\mathbf{P_a}$. Therefore, the catalytic cycle leading to $^{E}\mathbf{P_a}$ starting from $^{Z}\mathbf{P_a}$ should also be considered. Such an analogous isomerization has been previously reported by our group [50]. In this situation, it is believed that, after $^{Z}\mathbf{P_a}$ is obtained in the first catalytic cycle, the LAu^{+} catalyzed reaction would diverge into two competitive cycles (Fig. 3): either the annulation of **1A** with **B** to furnish $^{Z}\mathbf{P_a}$ (black line) or the *Z*-*E* isomerization of $^{Z}\mathbf{P_a}$ to generate $^{E}\mathbf{P_a}$ (red line). It is seen from Fig. 3 that the highest stationary point resulting in $^{E}\mathbf{P_a}$, C^6=C^7 rotation transition state **TS9-10**, is remarkably less stable than **TS1-2** resulting in $^{Z}\mathbf{P_a}$ in free energy (-64.7 vs -73.8 kcal/mol). Furthermore, the energy demand via **TS9-10** is as high as 30.1 kcal/mol. These observations indicate

that, once formed, $^{Z}\mathbf{P_a}$ is very unlikely to transform into $^{E}\mathbf{P_a}$ even with **1A** present.

3.2 Reactions on H-Substituted Substrate 2A.

As mentioned in the introduction, upon replacement of the cyclopropyl substituent by a hydrogen atom, the product-selectivity switches to produce the *E*-configured enone $^{E}\mathbf{P_b}$ as the sole product. Thus, further calculations are required to reveal the origin of the opposite chemoselectivity.

For the system starting with **2A**, we initially imitated the reaction from **1A** to perform detailed calculations for the formation of the *Z*-configured enone $^{Z}\mathbf{P_b}$ and the *E*-configured enone $^{E}\mathbf{P_b}$, which are given in Fig. 4 and 5. It was found that the reaction follows a similar mechanism to the **1A** system discussed above. Interestingly, unlike the difficulty of $^{Z}\mathbf{P_a}\rightarrow$ $^{E}\mathbf{P_a}$ in Fig. 3, the transformation from $^{Z}\mathbf{P_b}$ to $^{E}\mathbf{P_b}$ is much easier with a barrier of 22.5 kcal/mol (the difference between **TS19-20** and **IM19** in Fig. 5). In this case, once the substrate **2A** is used up, $^{Z}\mathbf{P_b}$ would evolve into $^{E}\mathbf{P_b}$ due to the stability of **TS11-12** resulting in $^{Z}\mathbf{P_b}$ over **TS19-20**. In other words, the alternative pathway leading to $^{E}\mathbf{P_b}$ needs to go through $^{Z}\mathbf{P_b}$. Besides, we also theoretically examined the speculation of Liu's group in Scheme 2 [22], in which the reaction proceeds via the Au-π-3-yn-1-imine intermediate **8**, followed by a quick C^6=C^7 rotation and subsequent nucleophilic cyclization, to give $^{E}\mathbf{P_b}$. Unfortunately, the energy barrier for **8** formation, 36.3 kcal/mol (the difference between **TS14'-8** and **IM14** in Fig. S6 in the Supporting Information), is very high, which is inaccessible under the given conditions. Therefore, the pathway via **8** is ruled out theoretically and subsequent evolvement into $^{E}\mathbf{Pb}$ from **8** was not evaluated further.

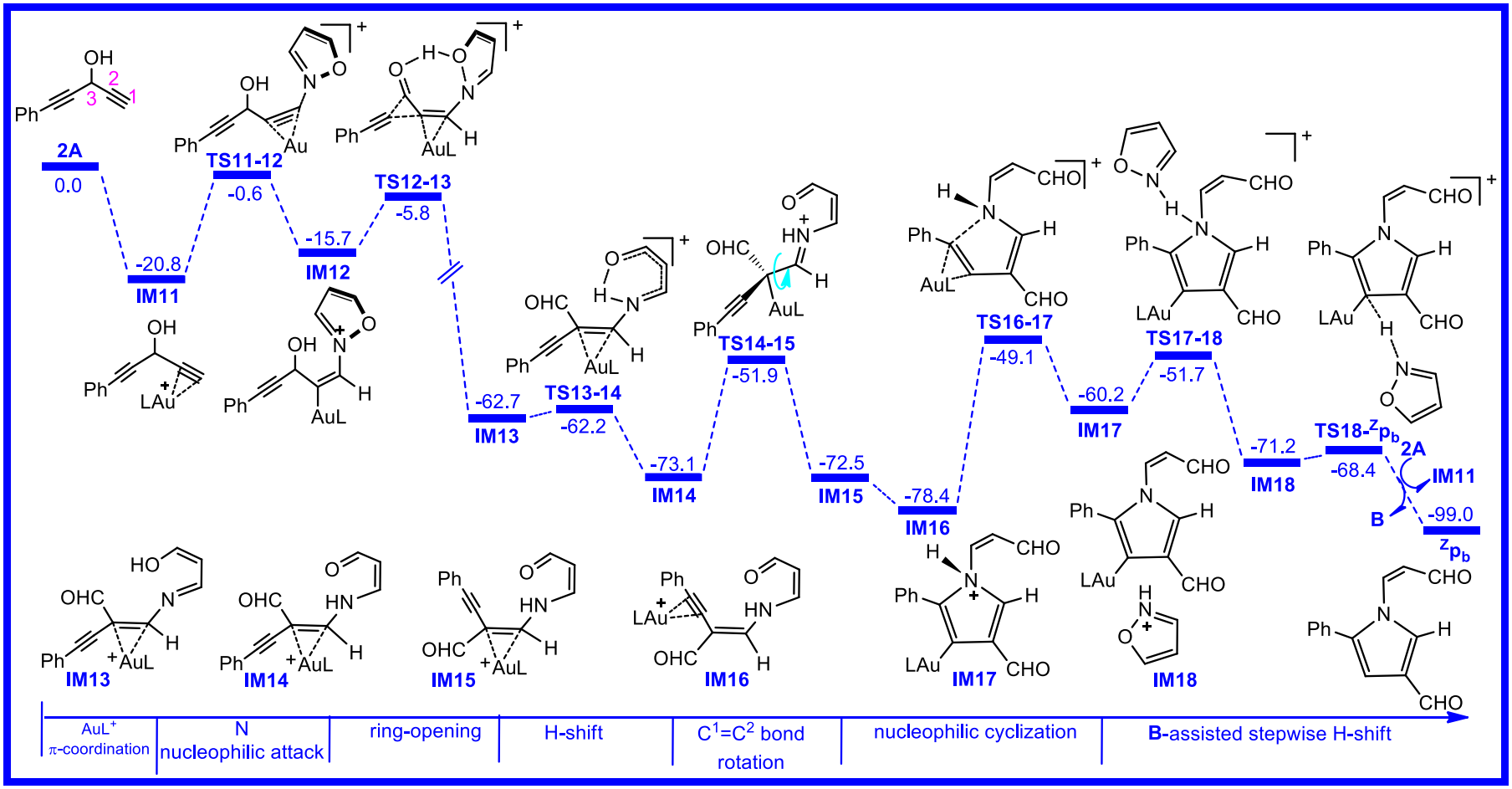

Fig. 4. Calculated free energy profile in DCE solvent for forming $^{Z}\mathbf{P_b}$ from the H-substituted 1,4-diyn-3-ol **2A** established in the present work. The relative free energies are given in kcal/mol. L = IPr

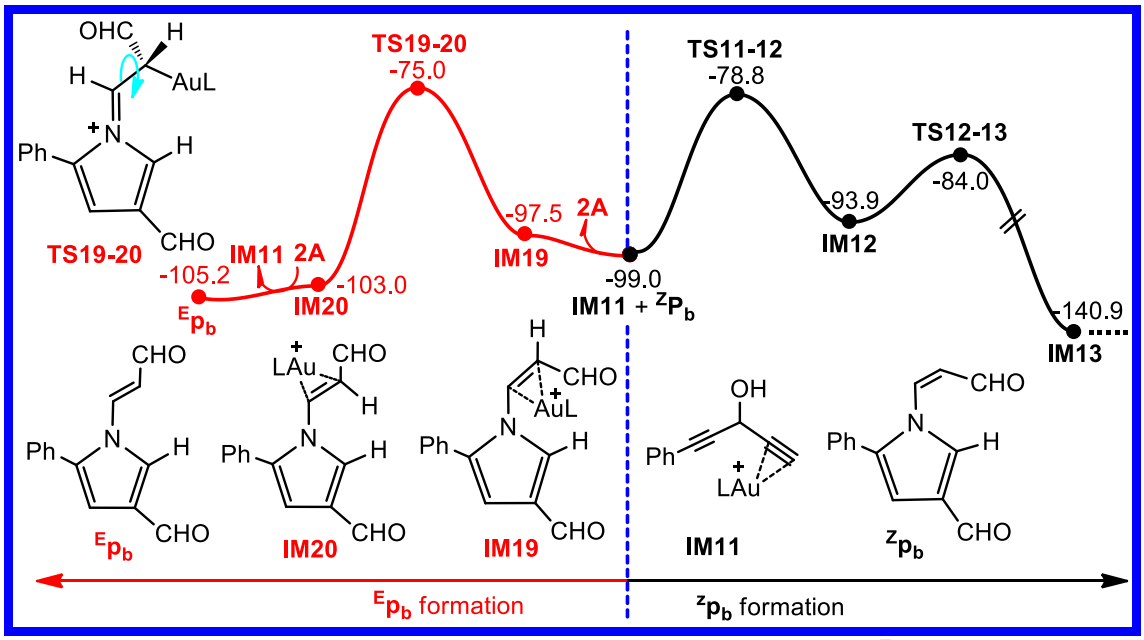

Fig. 5. Calculated free energy profiles in DCE solvent for forming ^{Z}**P**$_{b}$ (black line) and ^{E}**P**$_{b}$ via ^{Z}**P**$_{b}$ (red line), respectively. The relative free energies are given in kcal/mol. L = IPr

The mechanism in Fig. 5 indicates that the formation of ^{E}**P**$_{b}$ needs to go through ^{Z}**P**$_{b}$. Alternatively, avoidance of the ^{Z}**P**$_{b}$ intermediate allows us to design a new mechanism leading to ^{E}**P**$_{b}$, which also begins with **IM14** and features a double carbon-carbon double-bond rotation assisted by LAu^{+}. It can be seen in Fig. 6, with the coordination isomerization of **IM14**, the adduct **IM21** is formed in which the C^{6}=C^{7} bond is activated by LAu^{+}. The activated C^{6}=C^{7} bond then undergoes a rotation via **TS21-22**, leading to the species **IM22**. Immediately, LAu^{+} turns to coordinate with the C^{1}=C^{2} bond. The resultant isomer **IM23**, through **TS23-24**, performs the C^{1}=C^{2} rotation to give **IM24**, which posseses the same *E*-configured enone moiety as ^{E}**P**$_{b}$. It is noteworthy that the rotation step has an activation barrier of 18.0 kcal/mol and results in an overall barrier of 25.6 kcal/mol (difference between **TS23-24** and **IM22**). In contrast, the barrier for the C^{7}=C^{8} rotation via **TS21-22** is 18.8 kcal/mol. Obviously, the instability of the precursor intermediate **IM23** is of importance for the difficult C^{1}=C^{2}

bond rotation via **TS23-24**. To be ready for the following nucleophilic attack, LAu^+ is required to activate the alkynyl moiety. Thus, the coordination isomerization of **IM24** occurs to afford **IM25**. Subsequently, similar to **IM17** → ^{Z}**P$_b$** in Fig. 4, the reaction proceeds via N-nucleophilic attack of the C^5 atom followed by a **B**-assisted H-shift, eventually providing the product ^{E}**P$_b$** with the dissociation of LAu^+.

From the potential energy profile shown in Fig. 6, we can clearly see that the highest stationary point leading to ^{E}**P$_b$** corresponds to **TS25-26**, which is 2.7 kcal/mol greater than **TS16-17** leading to ^{E}**P$_b$** via ^{Z}**P$_b$** in Fig. 5. Using the Eyring equation, a 2.7 kcal/mol energy difference gives a ratio of 99/1, demonstrating the pathway with no involvement of ^{Z}**P$_b$** to be a preferred mechanism for ^{E}**P$_b$** formation.

3.2 Origins of Substituent-Controlled Chemoselectivity

In order to better understand the origins of the different chemoselectivities resulting from the cyclopropyl and H substituents, we performed the analyses of four selectivity-determining transition states: **TS6-7** (leading to ^{Z}**P$_a$** in Fig. 2) vs **TS33-34** (leading to ^{E}**P$_a$** in Fig. S3, similar to the formation of ^{E}**P$_b$** in Fig. 6), and **TS16-17** (leading to ^{Z}**P$_b$** in Fig. 4) vs **TS25-26** (leading to ^{E}**P$_b$** in Fig. 6), which are re-optimized with M06 functional in DCE solvent to obtain more accurate results. All of the four stationary points are related to the five-membered ring closure. The calculated results are given in Fig. 7.

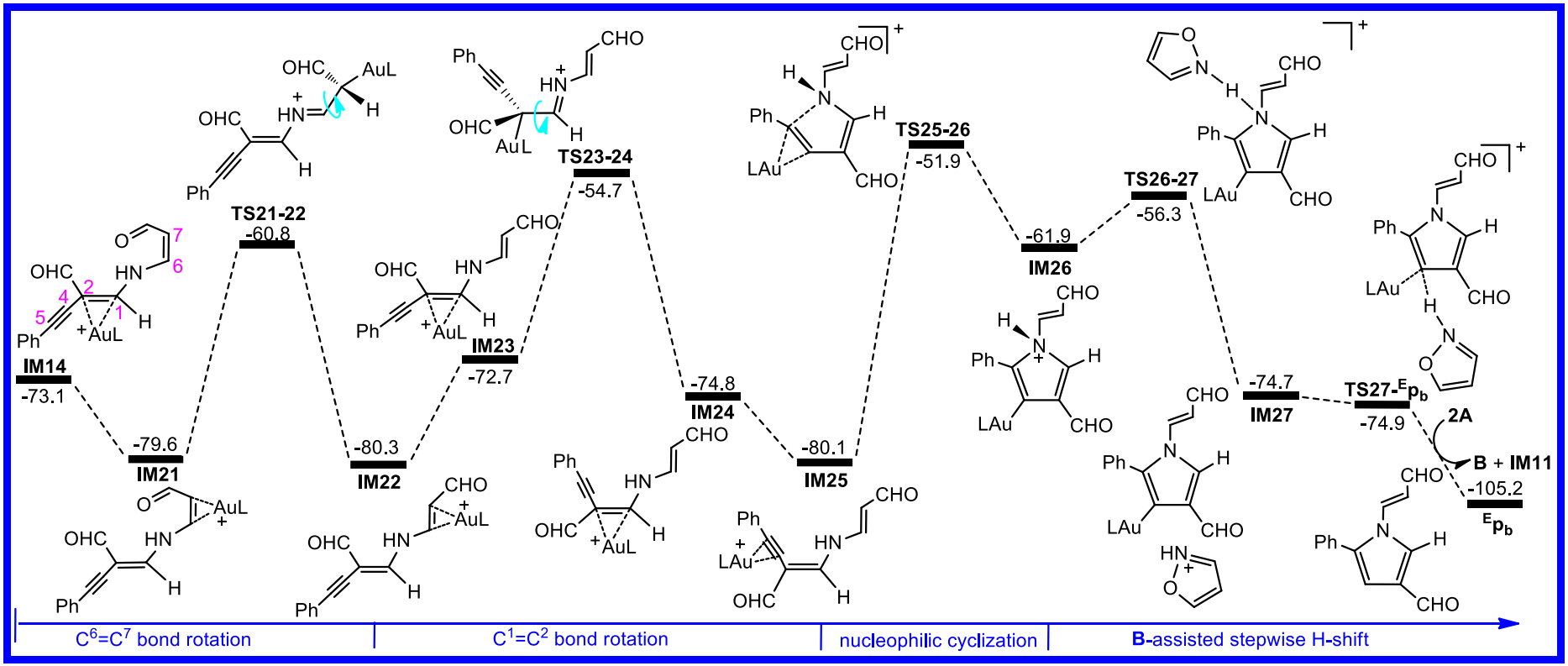

Fig. 6. Calculated free energy profile in DCE solvent for forming $^{E}\mathbf{P_b}$ from the intermediate **14** established in the present work. The relative free energies are given in kcal/mol. L = IPr

For the cyclopropyl-substituted system (left column), the free energy difference (ΔΔG) between **TS33-34** and **TS6-7** is 0.9 kcal/mol, corresponding to a ratio of 82:18 for $^{Z}\mathbf{P_a}/^{E}\mathbf{P_a}$. Since the counterion as a formal spectator [52-54] is not considered theoretically, the result derived from our computations is in qualitative agreement with the experimental observations regarding the 10:1 ratio for IPrAuCl/AgOTf catalysis and 4:1 for IPrAuCl/$AgSbF_6$ catalysis shown in Scheme 1. To gain insight into the *Z*/*E* chemoselectivity, we compared the electronic energies (ΔE, in parentheses) and entropy effects (reflected by $-T_{298k}\Delta S$, in brackets) of the two transition states. In comparison with the contribution of entropy effect (2.3 kcal/mol), **TS33-34** is found to have appreciably higher electronic energy than **TS6-7** (3.7 kcal/mol). Clearly, the structural stability of **TS6-7** plays a pivotal role in the selectivity preference. Furthermore, we performed the noncovalent interactions (NCIs) analyses [54, 55] to confirm the structural discrepancy of the two transition states. One can identify in Fig. 7 that a significant O···H—N hydrogen bonding interaction is present in **TS6-7**, but minimal interaction is observed in **TS33-34**. In summary, the O···H—N hydrogen bonding interaction in **TS6-7** creates an extra stabilization energy and thus results in **TS6-7** being appreciably lower in free energy than **TS33-34**.

As far as the H-substituted system is concerned, as exhibited in the right column of Fig. 7, **TS25-26** is 1.7 kcal/mol more stable than **TS16-17** in free energy. The resulting 1:94.6 ratio of the *Z*/*E* products is in rough accordance with the experimentally observed exclusively *E*-product [22]. We first compared the relative stability of **TS25-26** and **TS16-17** by looking at the electronic energies in parentheses. However, the given electronic energy change (2.0 kcal/mol) for the two transition states is inconsistent with the free energy difference (-1.7 kcal/mol), indicating that the structural stability is not a determining factor leading to the reversed chemoselectivity. Further

comparative analysis shows that the value of $-T_{298K}\Delta S$ in **TS25-26** is smaller than that in **TS16-17** with a difference of -2.8 kcal/mol, which overrides the electronic energy difference of 2.0 kcal/mol. Therefore, it is believed that the larger entropy effect in **TS25-26** leads to the overall preference to the free energy over **TS16-17**. In order to obtain additional support for this deduction, we analyzed the optimized geometric structures of **TS25-26** and **TS16-17**. As highlighted with solid green oval, because of the O···H—N hydrogen bonding interaction, **TS16-17** exhibits a more strained structure, thereby resulting in a smaller degree of disorder (ΔS). As a result, a larger value of $-T_{298K}\Delta S$ in **TS16-17** is achieved when compared to **TS25-26**. From an entropy perspective, one can easily understand the lower free energy of **TS25-26** relative to **TS16-17**.

One the other hand, the chemoselectivity is closely related to the capability of the $C^6=C^7$ double-bond rotation, which has an energy demand of 30.1 kcal/mol with cyclopropyl substituent (**IM9** → **TS9-10** in Fig. 4) and 22.5 kcal/mol with H substituent (**IM19** → **TS19-20** in Fig. 6). That is, under the given conditions, with cyclopropyl substitution, the obtained *Z*-configured enone cannot isomerize further into the *E*-configured enone. In order to explain this fact, we compared the geometric parameters of four key stationary points, including **IM9**, **TS9-10**, **IM19** and **TS19-20**. As seen in Table 1, the $\angle C^1\text{-N-}C^6$ changes from 120.4° in **IM9** to 130.7° in **TS9-10**. By comparison, for **IM19** to **TS19-20**, the corresponding bond angle varies insignificantly (128.5° vs 128.1°). It is likely that, to ensure the $C^6=C^7$ bond rotation, the bulky cyclopropyl group has to undergo a large structural twisting, which, as a result, produces an additional energy penalty in **TS9-10** and results in $^{\mathbf{Z}}\mathbf{P_a}$ as the final product.

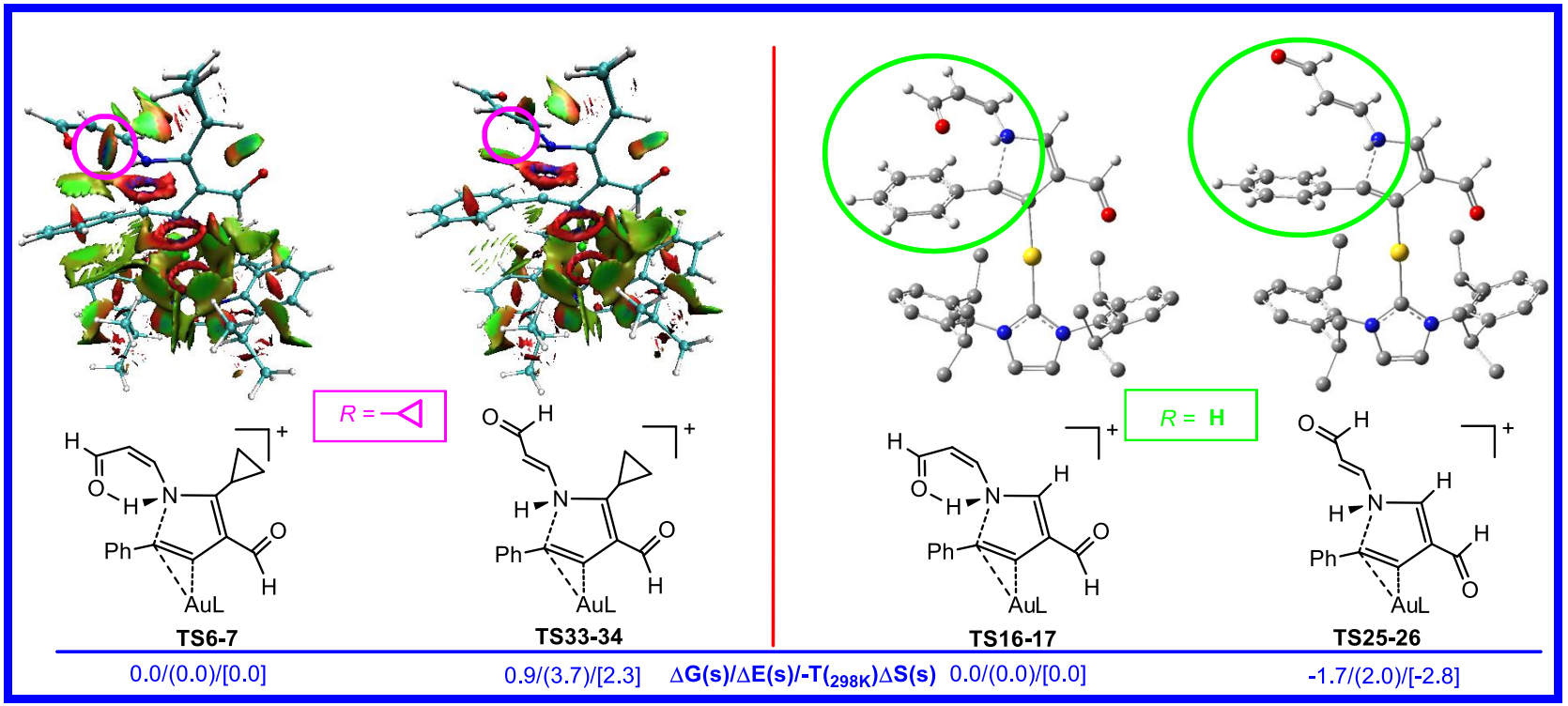

Fig. 7. Noncovalent interactions analyses for the chemoselectivity-determining TSs with cyclopropyl substituent (left column), optimized geometries for the chemoselectivity-determining TSs with H substituent (right column), as well as the Gibbs free energies, electronic energies (ΔE) in parentheses and entropy effect ($-T_{298k}\Delta S$) in square brackets in DCE solvent of the four TSs involved (marked with blue color). L = IPr

Table 1. Optimized geometrical parameters of **IM9** and **TS9-10** in Fig. 3, and **IM19** and **IM20** in Fig. 5. The bond distances and bond angles are given in Å and°, respectively. L = IPr

IM9	→	**TS9-10**	**IM19**	→	**TS19-20**
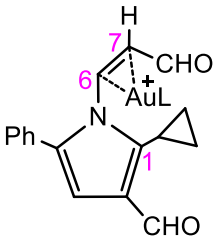		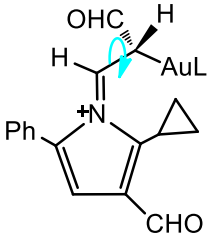	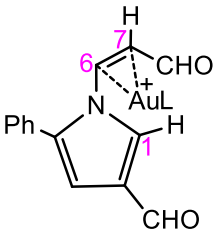		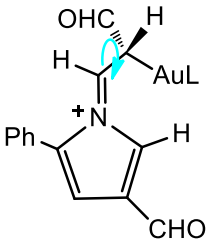
C7=C8 = 1.391		C7-C8 = 1.463	C7=C8 = 1.407		C7-C8 = 1.468
C7-N = 1.381		C7=N = 1.317	C7-N = 1.354		C7=N = 1.311
∠C6-C1-N = 121.2°		∠C6-C1-N = 123.4°	∠H-C1-N = 120.6°		∠H-C1-N = 120.6°
∠*C1-N-C7*= ***120.4***°		∠*C1-N-C7*= ***130.7***°	∠*C1-N-C7*= ***128.5***°		∠*C1-N-C7*= ***128.1***°
∠N-C7-C8 = 129.5°		∠N-C7-C8 = 123.4°	∠N-C7-C8 = 132.7°		∠N-C7-C8 = 130.8°

Overall, the substituent-induced divergent chemoselectivity originates from a combination of O···H—N hydrogen bonding interaction and ease of rotation of the C^6=C^7 double-bond. In the cyclopropyl system, the hydrogen bonding interaction enhances the stability of **TS6-7** leading to *Z*-configured enone, which is the final product due to large structural distortion caused by the bulky cyclopropyl group. With the H substituent, the presence of the hydrogen bonding interaction forces the structure of **TS16-17** to be strained, resulting in a decrease in order (ΔS). And ultimately, the *E*-configured enone is formed exclusively.

According to the calculated results above, we schematically display the integral catalytic cycles for the formation of $^{Z}\mathbf{P_a}$ and $^{E}\mathbf{P_b}$, respectively, in Scheme 3, which provides a consistent view of the mechanistic details for the annulation reactions with H- and cyclopropyl-substituents.

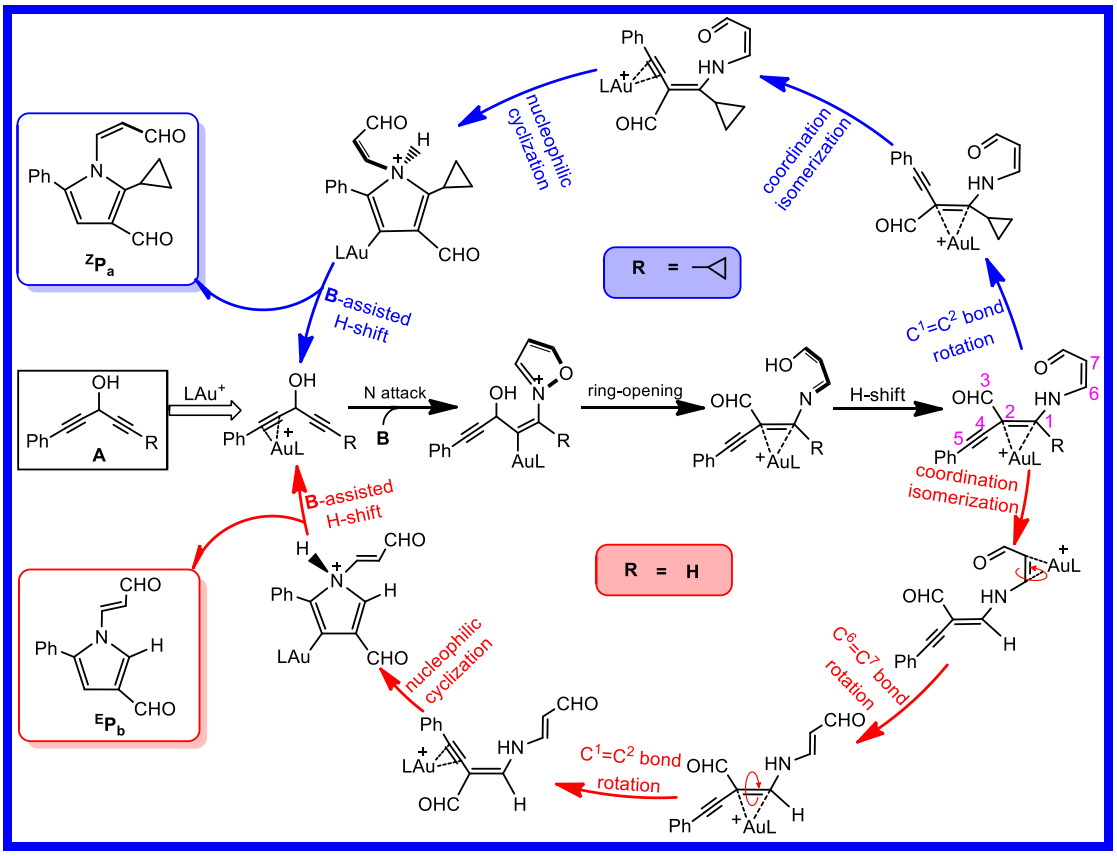

Scheme 3. A sketch of the catalytic cycles for forming $^{Z}\mathbf{P_a}$ and $^{E}\mathbf{P_b}$ from the Au(I)-catalyzed annulations of cyclopropyl- and H-substituted 1,4-diyn-3-ols with isoxazole **B**, respectively, based on the present calculations. L = IPr

4. Conclusions

The Au(I)-catalyzed [4+1] annulations of isoxazole (**B**) with cyclopropyl- and H-substituted 1,4-diyn-3-ols (i.e., **1A** and **2A**), respectively, have been computationally evaluated. Both reactions are initiated by LAu^{+} π-coordination to facilitate the N-nucleophilic attack of isoxazole **B**. A theoretical study indicates that the preferred nucleophilic position at non-phenylalkyne moiety over phenylalkyne moiety can be inherently attributed to the larger steric crowding involved in the N attack towards the phenylalkyne site.

After the nucleophilic attack, a concerted three-step forward product, obtained by

simultaneous isoxazole O-N cleavage, 1,2-phenylalkyne shift and the hydroxyl H shift was identified as a key intermediate, rather than the experimentally proposed iminogold carbene species. With the hydroxyl H migration to the N atom, the resultant nitrogen-hydride species favorably evolves either into $^{Z}\mathbf{P_a}$ for the **1A** system via $C^1=C^2$ rotation → nucleophilic cyclization → **B**-assisted protodeauration or into $^{E}\mathbf{P_b}$ for the **2A** reaction via two C=C rotations → nucleophilic cyclization → **B**-assisted protodeauration. Further theoretical investigations indicate that the chemoselective step is the nucleophilic cyclization but not the C=C double-bond rotation. The chemoselectivity for formation of $^{Z}\mathbf{P_a}$ can be explained as follows: (i) the additional O···H—N hydrogen bonding interaction helps to stabilize the cyclization transition state **TS6-7** leading to $^{Z}\mathbf{P_a}$ and (ii) a big structural deformation generated in the $^{Z}\mathbf{P_a}$ → $^{E}\mathbf{P_a}$ isomerization significantly increases the distortion penalty and thus leads to $^{Z}\mathbf{P_a}$ as the sole final product. In contrast, for the **2A** reaction, the chemoselectivity is reversed to provide the *E*-configured enone $^{E}\mathbf{P_b}$. It was found that the strained structure in the selective-controlled **TS16-17** leading to $^{Z}\mathbf{P_b}$ orders the system, which enables **TS25-26** to be lower in free energy than **TS16-17** and consequently results in the exclusive formation of $^{E}\mathbf{P_b}$.

The present theoretical results provide in-depth insights into the mechanisms and origins of regioselectivity and chemoselectivity of the title reactions and rationalizes the experimental observations.

Supporting Information

Figures giving calculated free energy profiles for other possible pathways in **1A**- and **2A**-involved systems and Cartesian coordinates and relative energies of all the species involved.

Acknowledgments

This work was jointly supported by the National Natural Science Foundation of China (Nos. 21773139 and 21473100), the Natural Science Foundation of Shandong Province (ZR2019MB016), the China Postdoctoral Science Foundation (2016M600531), and the Doctoral Start-Up Scientific Research Foundation of Qufu Normal University (Grant No. BSQD2012018).

References

[1] S. Thirumalairajan, B. M. Pearce, A. Thompson, Chem. Commun. 46 (2010) 1797–1812.

[2] J. C. P. Reyes, D. Romo, Angew. Chem. Int. Ed. 51 (2012) 6870–6873.

[3] H. Fan, J. Peng, M. T. Hamann, J. F. Hu, Chem. Rev. 108 (2008) 264–287.

[4] D. S. Kim, Y. S. Seo, C.H. Jun, Org. Lett. 17 (2015) 3842–3845.

[5] A. S. K. Hashmi, Chem. Rev. 107 (2007) 3180–3211.

[6] N. T. Patil, Y. Yamamoto, Chem. Rev. 108 (2008) 3395–3442.

[7] S. Abu Sohel, R.-S. Liu, Chem. Soc. Rev. 38 (2009) 2269–2281.

[8] M. E. Muratore, A. Homs, C. Obradors, A. M. Echavarren, Chem. Asian J. 9 (2014) 3066–3082.

[9] D. B. Huple, S. Ghorpade, R.-S. Liu, Adv. Synth. Catal. 358 (2016) 1348–1367.

[10] J. A. Lohrman, C.-L. Deng, T. A. Shear, L. N. Zakharov, M. M. Haley, D. W. Johnson, Chem. Commun. 55 (2019) 1919-1922.

[11] A. S. K. Raj, K. -C. Tan, L. -Y. Chen, M. -J. Cheng, R. -S. Liu, Chem. Sci. 10 (2019) 6437-6442.

[12] A. -H. Zhou, Q. He, C. Shu, Y. -F. Yu, S. Liu, T. Zhao, W. Zhang, X. Lu, L. -W. Ye, Chem. Sci. 6 (2015) 1265–1271.

[13] X.-Y. Xiao, A. -H. Zhou, C. Shu, F. Pan, T. Li, L.-W. Ye, Chem. Asian J. 10 (2015)

1854–1858.

[14] W. -B. Shen, X. -Y. Xiao, Q. Sun, B. Zhou, X. -Q. Zhu, J. -Z. Yan, X. Lu, L. -W. Ye, Angew. Chem. Int. Ed. 56 (2017) 605–609.

[15] H. Jin, L. Huang, J. Xie, M. Rudolph, F. Rominger, A. S. K. Hashmi, Angew. Chem. Int. Ed. 55 (2016) 794–797.

[16] H. Jin, B. Tian, X. Song, J. Xie, M. Rudolph, F. Rominger, A. S. K. Hashmi, Angew. Chem. Int. Ed. 55 (2016) 12688–12692.

[17] M. Chen, N. Sun, H. Chen, Y. Liu, Chem. Commun. 52 (2016) 6324–6327.

[18] Z. Zeng, H. Jin, J. Xie, B. Tian, M. Rudolph, F. Rominger, A. S. K. Hashmi, Org. Lett. 19 (2017) 1020–1023.

[19] W. Xu, G. Wang, N. Sun, Y. Liu, Org. Lett. 19 (2017) 3307–3310.

[20] R. L. Sahani, R.-S. Liu, Angew. Chem. Int. Ed. 56 (2017) 1026–1030.

[21] R. L. Sahani, R. -S. Liu, Angew. Chem. Int. Ed. 56 (2017) 12736 –12740.

[22] R. D. Kardile, B. S. Kale, P. Sharma, R. -S. Liu, Org. Lett. 20 (2018) 3806−3809.

[23] M. J. Frisch, G. W. Trucks, H. B. Schlegel, G. E. Scuseria, M. A. Robb, J. R .Cheeseman, G. Scalmani, V. Barone, B. Mennucci, G. A. Petersson, H. Nakatsuji, M. Caricato, X. Li, H. P. Hratchian, A. F Izmaylov, J. Bloino, G. Zheng, J. L. Sonnenberg, M. Hada, M. Ehara, K. Toyota, R. Fukuda, J. Hasegawa, M. Ishida, T. Nakajima, Y. Honda, O. Kitao, H. Nakai, T. Vreven, J. A. Montgomery, Jr. J. E.Peralta, F. Ogliaro, M. Bearpark, J. J. Heyd, E. Brothers, K. N. Kudin, V. N. Staroverov, R. Kobayashi, J. Normand, K. Raghavachari, A. Rendell, J. C. Burant, S. S. Iyengar, J. Tomasi, M. Cossi, N. Rega, J. M. Millam, M. Klene, J. E. Knox, J. B. Cross, V. Bakken, C. Adamo, J. Jaramillo, R. Gomperts, R. E. Stratmann, O. Yazyev, A. J. Austin, R. Cammi, C. Pomelli, J. W. Ochterski, R. L. Martin, K. Morokuma, V. G. Zakrzewski, G. A. Voth, P. Salvador, J. J. Dannenberg, S.

Dapprich, A. D. Daniels, O. Farkas, J. B. Foresman, J. V. Ortiz, J. Cioslowski, D. J. Fox, Gaussian 09, revision D.01; Gaussian, Inc., Wallingford, CT, 2009.

[24] C. Lee, W. Yangand, R. G. Phys. Rev. B 37 (1988) 785–789.

[25] B. Michlich, A. Savin, H. Stolland, H. Preuss, Chem. Phys. Lett. 157 (1989) 200–206.

[26] A. D. Becke, J. Chem. Phys. 98 (1993) 5648–5652.

[27] P. J. Stephens, F. J. Devlinand, M. J. Fnsch, J. Phys. Chem. 98 (1994) 11623–11627.

[28] G. Pei, Y. Liu, G. Chen, X. Yuan, Y. -Y. Jiang, S. Bi, Catal. Sci. Technol. 8 (2018) 4450–4462.

[29] Y. Yang, Y. Liu, P. Lv, R. Zhu, C. Liu, D. Zhang, J. Org. Chem. 83 (2018) 2763–2772.

[30] Y. Liu, Y. Tang, Y.-Y. Jiang, X. Zhang, P. Li, S. Bi, ACS Catal. 7 (2017) 1886–1896.

[31] X. Zhang, Y. Liu, G. Chen, G. Pei, S. Bi, Organometallics 36 (2017) 3739–3749.

[32] C. Liu, Y. Liu, Y. Tang, H. Liang, S. Bi, Org. Biomol. Chem. 14 (2016) 2522–2536.

[33] Y. Liu, X. Yang, L. Liu, H. Wang, S. Bi, Dalton Trans. 44 (2015) 5354–5363.

[34] M. Dolg, U. Wedig, H. Stoll, H. Preuss, J. Chem. Phys. 86 (1987) 866−872.

[35] D. Andrae, U. Hä ussermann, M. Dolg, H. Stoll, H. Preuss, Theor. Chim. Acta. 77 (1990) 123−141.

[36] K. Fukui, J. Phys. Chem. 74 (1970) 4161–4163.

[37] K. Fukui, Acc. Chem. Res. 14 (1981) 363–368.

[38] Y. Zhao, D. G. Truhlar, Theor. Chem. Acc. 120 (2008) 215–241.

[39] Y. Zhao, D. G. Truhlar, Acc. Chem. Res. 41 (2008) 157–167.

[40] J. Tomasi, M. Persico, Chem. Rev. 94 (1994) 2027–2094.

[41] V. Barone, M. Cossi and J. Tomasi, J. Comput. Chem. 19 (1998) 404–407.

[42] M. Cossi, V. Barone, R. Cammi, J. Tomasi, Chem. Phys. Lett. 255 (1996) 327–335.

[43] L. Falivene, V. Barone, G. Talarico, Molecular Catalysis 452 (2018) 138–144.

[44] F. Zarkoob, A. Ariafard, Organogmetallics 38 (2019) 489−497.

[45] J. Zhang, Q. Quan, Z. Lin, Z. Xie, Organometallics. 33 (2014) 3556–3563.

[46] L. J. Song, T. Wang, X. Zhang, L. W. Chung, Y. D. Wu, ACS Catal. 7 (2017) 1361–1368.

[47] T. Sperger, C. M. Le, M. Lautens, F. Chem. Sci. 8 (2017) 2914–2922.

[48] W. Guo, Y. Xia, J. Org. Chem. 80 (2015) 8113−8121.

[49] W. Wu, S. Bi, Y. Liu, Y. Tang, B. Li, Org. Biomol. Chem. 13 (2015) 11539−11549.

[50] L. Liu, G. Pei, P. Liu, B. Ling, Y. Liu, S. Bi, J. Org. Chem. 83 (2018) 2067–2076.

[51] H. -Z. Yu, Y. Fu, Z. -Q. Zhang, Q. Zhang, ACS Catal. 6 (2016) 798–808.

[52] I. V. Alabugin, M. E. Krafft, D. V.Vidhani, J. Am. Chem. Soc. 138 (2016) 2769–2779.

[53] W. Fang, Y. Wei, X. -Y. Tang, M. Shi, Chem. Eur. J. 23 (2017) 6845– 6852.

[54] T. Lu, F. Chen, J. Comput. Chem. 33 (2012) 580–592.

[55] S. Manzetti, T. Lu, J. Phys. Org. Chem. 26 (2013) 473–483.

Table of Contents Graphic